Green Chemistry

PAPER

Check for updates

Ionothermal carbonization of sugarcane bagasse in imidazolium tetrachloroferrate ionic liquids: effect of the cation on textural and morphological properties†

Soha Aldroubi,[a] Mohamed El-Sakhawy,[b] Samir Kamel,[b] Peter Hesemann, [iD] [a] Ahmad Mehdi [iD] *[a] and Nicolas Brun [iD] *[a]

The valorization of abundant agrowastes into chemicals and advanced materials is of key importance in the context of the circular bioeconomy and biorefinery. Herein, we report the ionothermal carbonization (ITC) of sugarcane bagasse, a fibrous residue made of lignocellulose, to engineer advanced carbonaceous materials, namely ionochars. We prepared a series of imidazolium tetrachloroferrate ionic liquids (IL) bearing modular substituents, *e.g.*, alkyl chains with different lengths or benzyl groups. The effect of the cation on both textural and morphological properties is highlighted. Ionochars with high specific surface area (up to 800 m^2 g^{-1}), tuneable pore volume (up to 0.8 cm^3 g^{-1}), singular nanostructures and adjustable CO_2 uptake/retention were obtained.

1. Introduction

Lignocellulosic agricultural wastes are abundant and renewable resources that can be used as feedstocks for the production of fuels, platform molecules and materials.[1] Sugarcane bagasse is one of those agricultural residues produced in large quantities in sugar factories by grinding sugarcane. This fibrous agrowaste is mainly constituted of cellulose, hemicellulose and lignin. Bagasse comprises low-density fibers with a very wide particle size distribution.[2] Burning bagasse to meet the internal energy needs of sugar mills remains wasteful and inefficient.[3] A part of the surplus is used in the production of animal feed and in the manufacture of paper and board.[3] Besides, the valuation of bagasse can be carried out by carbonization[4] or activation[5] to convert it into gas, bio-oils, biochars or other advanced carbonaceous materials.

Amongst carbonization processes, the hydrothermal carbonization (HTC) has been reported as a profitable, atom efficient and environmentally safe process.[6] HTC has been widely studied and several pilot and industrial-scale plants have been developed.[7] HTC consists in converting organic matter, typically agrowaste or sewage sludge, into carbonaceous materials at mild processing temperature (<250 °C), in water and under autogenous pressure (<20 bars).[8–10] When applied to lignocellulosic agrowastes, very complex cascade reactions of hydrolysis, dehydration, decarboxylation, polymerization, and aromatization take place.[11] Firstly, holocellulose (*i.e.*, hemicellulose and cellulose) hydrolyzes yielding monosaccharides, mainly xylose and glucose. This first step usually occurs at high temperatures, above 200 °C, and is limited at the lignocellulose–water interface. Secondly, glucose and xylose dehydrate to 5-hydroxymethylfurfural (HMF) and furfural, respectively. Further degradation of the furfural derivatives can generate organic acids, resulting in a decrease of the pH, and thus accelerating dehydration reactions. Finally, the furfural intermediates eventually condense to form furan-rich materials, namely hydrochars. At higher temperature (>220 °C), the aromatic character increases, with a low fraction of carboxyl and carbonyl groups. Due to weak dissolution in water, the lignocellulose–water interface is limited. As a direct consequence, HTC mainly occurs through intramolecular reactions, yielding non-porous hydrochars with poor textural and morphological control. Thus, HTC usually involves the use of sacrificial additives and templates, making the whole process costly and inefficient.[12]

Ionic liquids (ILs) are of great importance in modern chemistry,[13] especially in the field of biomass processing and biorefinery.[14] ILs are defined as salts that are liquid at a temperature below 100 °C and that usually consist of an organic cation

[a] *ICGM, Univ. Montpellier, CNRS, ENSCM, Montpellier, France.*
E-mail: nicolas.brun@enscm.fr, ahmad.mehdi@umontpellier.fr
[b] *Cellulose and Paper Department, National Research Centre, Giza, Egypt*

in interaction with an inorganic anion. ILs are considered as green solvents[15] due to singular properties such as: (i) almost zero vapor pressure which prohibits any evaporation in the atmosphere; (ii) non-flammability; and (iii) in many cases, high thermal stability, which offers potential recyclability and reusability.[16] ILs demonstrated good ability for the dissolution and/or selective depolymerization of cellulose,[17–19] lignin[20,21] and even lignocellulosic agrowastes, including sugarcane residues.[22] The dissolution of lignocellulose has been demonstrated in particular with ILs bearing a cation with short alkyl chains[23] and an anion with strong hydrogen-bond acceptance;[24] 1-butyl-3-methylimidazolium chloride ([C$_4$mim]Cl) being the most widely reported in the literature.[17] Beyond dissolution, depolymerization and derivatization, ILs were used as recyclable solvents for the carbonization of simple carbohydrates,[25–27] polysaccharides[28] and raw lignocellulosic agrowastes,[27,29–31] including sugarcane bagasse.[31] This thermochemical process, known as ionothermal carbonization (ITC), must be considered as a relative of the HTC process and allows engineering advanced carbonaceous materials, namely ionochars. In particular, 1-butyl-3-methylimidazolium tetrachloroferrate ([C$_4$mim]FeCl$_4$) demonstrated advantageous features in ITC.[29,30] Besides strong magnetic field response,[32,33] and local ordering of its magnetic anion,[34] [C$_4$mim]FeCl$_4$ displays an intermediate Lewis acidity[35,36] and a relatively high thermal stability compared to [C$_4$mim]Cl. It was demonstrated that [C$_4$mim]FeCl$_4$ catalyses both (i) the depolymerization of lignin through γ-O ester bond cleavage;[20] and (ii) the dehydration and polycondensation reactions involved during solvothermal carbonization, yielding ionochars with a more pronounced aromatic aspect with respect to analogous hydrochars.[25] In a previous study, our group demonstrated the beneficial inputs of [C$_4$mim]FeCl$_4$ in the ITC of a wet agrowaste, i.e., cocoa bean shells, yielding highly porous ionochars with high mass and carbon yields.[30] While the role of the anion (i.e., Cl$^-$, FeCl$_4^-$, BF$_4^-$ and Tf$_2$N$^-$) associated with [C$_4$mim]$^+$ was clearly evidenced in the literature,[30,31] the way the structure of the imidazolium cation affects the ITC of lignocellulose has not been explored yet and is still open to discussion. Herein, we focus on the systematic evaluation of the cationic structure to assess its effect on the ITC of sugarcane bagasse.

2. Experimental section

2.1. Materials

Sigmacell cellulose (type 50, 50 μm), 1-ethyl-3-methylimidazolium chloride (99%), 1-butyl-3-methylimidazolium chloride (99%), 1-hexyl-3-methylimidazolium chloride, and 1-octyl-3-methylimidazolium chloride were purchased from IoLiTec (Germany). Sodium chloride (NaCl, 99%), potassium chloride (KCl, 99%), iron(III) chloride hexahydrate (FeCl$_3$·6H$_2$O, 97%), 1-methylimidazole (C$_4$H$_6$N$_2$, 99%), 1-butylimidazole (C$_7$H$_{12}$N$_2$, 99%), benzyl chloride (C$_6$H$_5$CH$_2$Cl, 99%), imidazole (C$_3$H$_4$N$_2$, 99%) and sodium hydride (NaH, 60% dispersion in mineral oil) were purchased from Sigma Aldrich. Depithed

and washed sugarcane bagasse (Bg) was donated by Quena Company for Paper Industry (Egypt). Sugarcane was previously pressed to extract the juice, ground and sieved to separate the pith. After depithing, Bg was washed three times with water (Bg : water mass ratio of 1 : 10) to separate residual sugar and impurities. After each washing, Bg was dewatered to a dry content of 20–25 wt%. Finally, Bg was dried in a convection oven at 100 °C for 8 h, ground and sifted (>100 μm). An ash content below 2 wt% was determined by thermogravimetric analysis in air up to 800 °C. All the other reagents were used without further purification.

2.2. Preparation of the tetrachloroferrate ionic liquids and salts

We prepared a series of imidazolium tetrachloroferrate ILs bearing modular side groups, e.g., alkyl chains with different lengths (from C$_2$ to C$_8$; Fig. 1a) and/or benzyl groups (Bn; Fig. 1b). The four 1-alkyl-3-methylimidazolium tetrachloroferrate ionic liquids (ILs) of the [C$_x$mim]FeCl$_4$ series (with x = 2, 4, 6 or 8) were synthesized by adapting a procedure reported in the literature.[37] In a typical synthesis, the analogous 1-alkyl-3-methylimidazolium chloride [C$_x$mim]Cl was mixed in an equimolar amount with iron(III) chloride hexahydrate. The mixture was heated at 80 °C under stirring for 6 hours. At the end of the reaction, two phases were obtained: a lower phase comprising the expected 1-alkyl-3-methylimidazolium tetrachloroferrate IL and an aqueous upper phase. Water was removed via rotary evaporation at 60 °C and 10 mbar for 4 hours and subsequent lyophilization for 12 hours. [(Bn)mim]FeCl$_4$, [(Bn)bim]FeCl$_4$ and [(Bn)$_2$im]FeCl$_4$ were prepared following the same procedure, using [(Bn)mim]Cl, [(Bn)bim]Cl and [(Bn)$_2$im]Cl (synthesis details described in ESI†) as precursors. NaFeCl$_4$ and KFeCl$_4$ were prepared based on the procedures described in the literature.[38] NaCl and KCl anhydrous salts were mixed with FeCl$_3$·6H$_2$O in a 1 : 1 molar ratio, stirred for 5 hours and heated to 165 and 240 °C respectively. Water was removed via rotary evaporation at 60 °C and 10 mbar for 4 hours followed by freeze-drying for 12 hours. Melting points of NaFeCl$_4$ (163 °C) and KFeCl$_4$ (240 °C) were determined with a Büchi B-540 melting point apparatus.
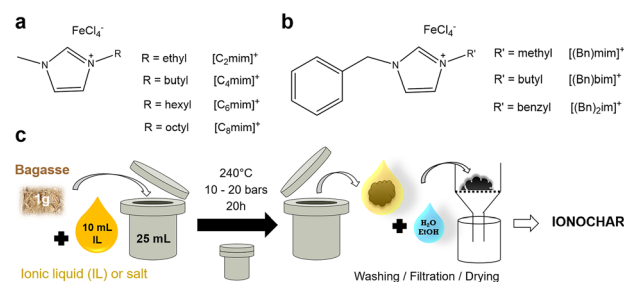
Fig. 1 Chemical structure of the different ILs studied herein. (a) 1-Alkyl-3-methylimidazolium tetrachloroferrate ILs bearing alkyl chains with different lengths (from ethyl, C$_2$, to octyl, C$_8$). (b) Imidazolium-based tetrachloroferrate ILs bearing benzyl groups (Bn). (c) Schematic representation of the ionothermal carbonization process (ITC).

2.3. Carbonization of sugarcane bagasse and cellulose

Ionothermal carbonization (ITC) of sugarcane bagasse was performed using the same protocol as described by Cibien, Parot et al.[30] Typically, 1.0 g of ground and sifted bagasse (>100 μm) was mixed with 40.2 mmol of IL or salt, sealed in a Teflon lined autoclave (23 mL) and heated at 240 °C for 20 h under autogenous pressure. After quenching in cold water and cooling down to room temperature, samples were washed once with ultrapure water (150 mL), once with a water/ethanol mixture (50 : 50, v/v) (150 mL) and once with pure ethanol (150 mL), filtered, and dried at 80 °C overnight in a vacuum drying oven (Fig. 1c). The ionochars prepared in the $[C_x\text{mim}]$ FeCl_4 series were named **C_xm-Bg**. The ionochars prepared in $[(\text{Bn})\text{mim}]\text{FeCl}_4$, $[(\text{Bn})\text{bim}]\text{FeCl}_4$ and $[(\text{Bn})_2\text{im}]\text{FeCl}_4$ were named **(Bn)m-Bg**, **(Bn)b-Bg** and **(Bn)$_2$-Bg**, respectively. The ionochars prepared in NaFeCl_4 and KFeCl_4 were named **Na-Bg** and **K-Bg**, respectively. Similar ionothermal carbonization experiments were carried out with commercial cellulose; the ionochars were named **C_xm-C**.

Hydrothermal carbonization (HTC) in 10 mL of ultrapure water was also carried out on bagasse (1 g) under similar conditions, yielding the hydrochar named **HTC-Bg**. After washing and oven drying, blackish powders were collected and thoroughly characterized. Pyrochars were prepared by pyrolysis of ground and sifted bagasse (>100 μm) in a horizontal tube furnace under argon flow (50 mL min^{-1}). Three different thermal treatments were carried out at 350, 550 and 750 °C for 4 h with a heating rate of 1 °C min^{-1}, yielding **P350-Bg**, **P550-Bg** and **P750-Bg**, respectively. Blackish powders were directly collected and thoroughly characterized without any additional pre-treatment. All experiments were performed in duplicate without noting any significant difference regarding textural and morphological properties.

2.4. Characterization

The mass yield (eqn (1)) and the corrected mass yield (eqn (2)) were calculated as follows:

$$\text{Mass yield}(\%) = \frac{m_{\text{dried char}}(g)}{m_{\text{dried biomass}}(g)} \times 100 \quad (1)$$

$$\text{Corr. mass yield}(\%) = \frac{m_{\text{dried char}}(g) - m_{\text{residual atoms}}(g)}{m_{\text{dried biomass}}(g)} \times 100 \quad (2)$$

with $m_{\text{dried char}}$, $m_{\text{dried biomass}}$ and $m_{\text{residual atoms}}$, the masses of the dried char (pyrochar, hydrochar or ionochar), the dried initial biomass and the mass of residual atoms, respectively. Residual atoms correspond to any atom present in the dried char and coming from the salt (FeCl_3) or the ionic liquid ($[\text{Bmim}]\text{Cl}$ or $[\text{Bmim}]\text{FeCl}_4$), i.e., iron, chloride and nitrogen excess. Iron and chloride contents were determined by SEM-EDX. The nitrogen content was determined by elemental analysis. The nitrogen excess originating from the ionic liquid was determined by subtracting the nitrogen coming from the initial biomass. HTC-Bg was used as a reference.

The carbon yield (eqn (3)) was calculated as follows:

$$\text{Carbon yield}(\%) = \text{Mass yield}(\%) \times \frac{C_{\text{dried char}}(\text{wt}\%)}{C_{\text{dried biomass}}(\text{wt}\%)} \times 100 \quad (3)$$

with $C_{\text{dried char}}$ and $C_{\text{dried biomass}}$, the carbon contents in the dried char and the dried initial biomass, respectively.

Combustional elemental analyses (C, H, N, O) were performed on a vario MICRO cube analyzer from Elementar. FTIR spectroscopy was performed in attenuated total reflectance (ATR) mode on a PerkinElmer Spectrum Two spectrometer. ^{13}C solid-state NMR was made on a VARIAN VNMRS 300 MHz spectrometer at 75.44 MHz. A VARIAN T3 MAS probe was used with 3.2 mm ZrO_2 rotors. Experiments were done using cross polarization magic angle (CP-MAS) with a contact time of 1 ms and a recycle delay of 5 s and a rotor speed of 15 kHz. GC-MS was performed on a Shimadzu QP2010SE gas chromatograph-mass spectrometer with a Phenomenex Zebron ZB-5 ms column (30 m × 0.18 mm × 0.18 μm). Injection: split 1 : 30@250 °C. Oven program: 50 °C (hold 2 min) 50–280 °C at 22 °C min^{-1} (hold 2 min). Raman spectroscopy was carried out on a Renishaw inVia Raman microscope with a 532 nm laser excitation. Scanning electron microscopy (SEM) analyses were performed on a Hitachi S-4800 electron microscope. SEM-EDX (Energy Dispersive X-ray spectroscopy) analyses were performed on a Zeiss EVO HD15 electron microscope. Transmission electron microscopy (TEM) analyses were performed on a JEOL 1200 microscope from the MEA platform, Université de Montpellier. N_2 (at 77 K) and CO_2 (at 273, 298 and 323 K) physisorption experiments were carried out on a Micromeritics 3Flex apparatus. Ionochars and hydrochars were degassed at 150 °C for 6 h under high vacuum (ca. 0.1 Pa) before physisorption measurements. Pyrochars were degassed at 300 °C for 24 hours under high vacuum (ca. 0.1 Pa) before physisorption measurements. To determine the isosteric heats of adsorption, we applied the Clausius–Clapeyron equation (see eqn (4) below) to CO_2 adsorption isotherms obtained at the three different temperatures.

$$\Delta H_{\text{ads}} = R\left(\frac{\partial \ln p}{\partial \frac{1}{T}}\right)_\theta \quad (4)$$

with R, the molar gas constant ($R = 8.314$ J mol^{-1} K^{-1}); Θ, the recovery rate, i.e., the fraction of active sites occupied by the CO_2 molecules or mmol of CO_2 adsorbed per gram of ionochar; T, the temperature, K; and p, the absolute pressure, kPa.

3. Results and discussion

The ITC of sugarcane bagasse was first performed in four 1-alkyl-3-methylimidazolium tetrachloroferrate ILs with various alkyl chain lengths (Fig. 1a).[37,39] The as-obtained ionochars were named **C_2m-Bg**, **C_4m-Bg**, **C_6m-Bg** and **C_8m-Bg**, respectively. The nitrogen sorption isotherms obtained at 77 K for these four ionochars display type I/II isotherms with a H4-

type hysteresis loop (Fig. 2a), characteristic of porous materials with micro-, meso- and macropores. The shape of the isotherms changes significantly from C_8m-Bg to C_2m-Bg, with a higher volume of nitrogen adsorbed at high relative pressure. This feature reflects an increase in the contribution of the external pore volume (Fig. 2b), that is the interparticle void spaces that can be seen as a continuum of meso- and macropores. When decreasing the length of the alkyl chain, the BET-equivalent specific surface area (SSA_{BET}) gradually increases from 173 m^2 g^{-1} for C_8m-Bg to 734 m^2 g^{-1} for C_2m-Bg (Table S1† and Table 1). A similar trend is observed regarding pore volume that gradually increases from 0.12 cm^3 g^{-1} for C_8m-Bg to 0.84 cm^3 g^{-1} for C_2m-Bg (Fig. 2b and Table 1).

The length of the alkyl chain has, however, no effect on both mass (between 50.8 wt% and 52.6 wt%) and carbon yields (between 78.1 wt% and 81.9 wt%) which are very similar in the C_xm-Bg (with x = 2, 4, 6, or 8) series (Table S2† and Table 1). The four ionochars of the C_xm-Bg series exhibit similar infrared spectra regardless of the length of the alkyl

Fig. 2 (a) Nitrogen sorption isotherms at 77 K and (b) total, external and micropore volumes of the four ionochars obtained in 1-alkyl-3-methyl-imidazolium tetrachloroferrate ILs with various alkyl chain lengths from ethyl, C_2, to octyl, C_8. (c) Total, external and micropore volumes of C_2m-Bg, K-Bg, Na-Bg and HTC-Bg.

chain (Fig. 3a). The four spectra show an intense band at 1700 cm^{-1}, which is characteristic of the stretching vibrations of the C=O bonds of aromatic carbonyl groups ($\nu_{C=O}$). Two bands centered at 1600 cm^{-1} and 1440 cm^{-1} correspond to the C=C bond of aromatic groups ($\nu_{C=C}$). A broad band between 1220 and 1280 cm^{-1} results from the stretching of the C–O bonds of aromatic ether and ester groups (ν_{C-O}). In addition, a weak band centered at 1374 cm^{-1}, corresponding to the deformation δ_{CH_3}, suggests the presence of aromatic methyl groups.

We also studied (i) the HTC of sugarcane bagasse in ultra-pure water, yielding the hydrochar named **HTC-Bg**, and (ii) the conventional pyrolysis of sugarcane bagasse under argon flow at three temperatures, *i.e.*, 350, 550 or 750 °C, yielding pyrochars named **P350-Bg**, **P550-Bg** and **P750-Bg**, respectively. On the one hand, the hydrochar displays a type III isotherm typical of nonporous (or macroporous) materials (Fig. S1, Table S3† and Table 1). On the other hand, the two pyrochars **P550-Bg** and **P750-Bg** display type I isotherms typical of microporous materials (Fig. S2†). Note that the pyrochar **P350-Bg** displays a type III isotherm (Fig. S2†), supporting the absence of micropores or the presence of narrow micropores with poor accessibility. To confirm these features, we performed carbon dioxide sorption isotherms at 273 K on the three pyrochars (Fig. S2† and Table 1). The specific surface areas determined by carbon dioxide sorption at 273 K are systematically higher than the ones determined by nitrogen sorption at 77 K. This feature supports the presence of ultra-micropores, *i.e.*, narrow micropores with an effective pore width below 0.7 nm (Fig. S2c and d†), which are more readily accessible due to kinetics that is more favorable at 273 K than at 77 K and the kinetic diameter of carbon dioxide molecules that is slightly smaller as compared with nitrogen. This result is in good agreement with the literature. Usually, sugarcane bagasse-derived pyrochars treated at moderate temperatures (below 500 °C) display limited specific surface areas and low pore volumes mainly attributed to narrow micropores.[4] These features highlight the singularity of ITC compared to HTC and conventional pyrolysis. Achieving textural properties comparable to those obtained herein with ionochars (above 700 m^2 g^{-1} and 0.8 cm^3 g^{-1}) would require harsher conditions together with the generation of a large amount of waste to be treated. Indeed, it usually involves liquid impregnation with activating agents such as H_3PO_4 or NaOH, oven-drying for several hours above 80 °C, subsequent thermal treatment above 750 °C for at least 1 hour, and intensive washing with water before final oven-drying for several hours above 80 °C.[5] Thus, ITC can be positioned as a potentially sustainable approach in terms of energy consumption, environmental factor and atom economy – provided that the synthesis of the aforementioned ILs also respects the precepts of green chemistry and that the ILs are reusable as shown in a previous study.[30] It is important to note that both elemental analyses performed on ionochars (Table S2† and Table 1) and GC-MS and FTIR (Fig. S3†) carried out on recovered ILs after ITC confirmed the good stability of the four imidazolium tetrachloroferrate ILs of the [$C_x$mim] FeCl₄ series, which display a decomposition temperature
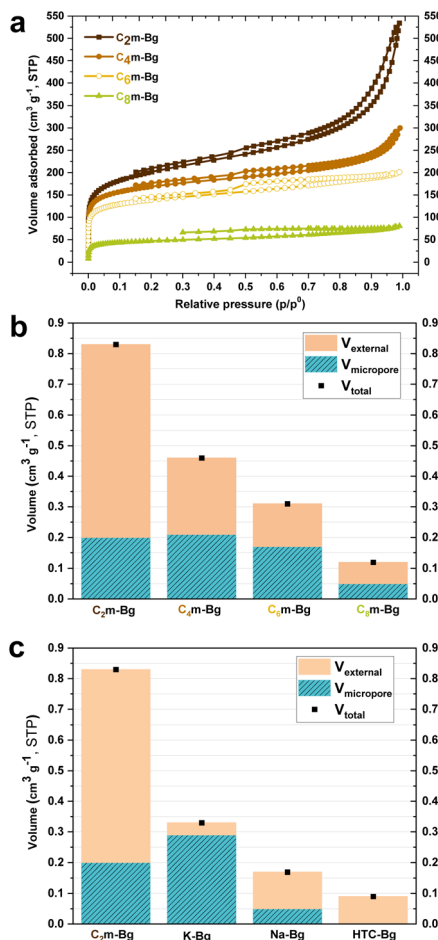
Table 1 Yields, elemental compositions and textural properties of the different iono-, hydro- and pyrochars reported herein

Chars	Y_{mc}^a (wt%)	Y_c^b (%)	C^c (wt%)	O/C^d	N/C^d	Fe^e (wt%)	Cl^e (wt%)	SSA_{BET} (m² g⁻¹)	SSA_{micro}^f (m² g⁻¹)	V_{total}^g (cm³ g⁻¹)	V_{ext}^f (cm³ g⁻¹)
C₂m-Bg	50.8	78.1	67.4	0.29	0.0026	2.3	1.7	734	467	0.83	0.63
C₂m-Bg-r1	51.3	80.7	69.6	0.23	0.0186	0.8	1.7	696	437	0.82	0.63
C₂m-Bg-r2	50.8	79.2	69.0	0.23	0.0261	1.0	1.4	701	390	1.05	0.88
C₄m-Bg	52.2	81.9	69.0	0.28	0.0044	1.2	2.4	628	495	0.46	0.25
C₆m-Bg	51.7	79.2	65.4	0.27	0.0040	3.9	2.7	518	396	0.31	0.14
C₆m-Bg-r1	48.2	75.4	70.4	0.23	0.0281	0.4	1.0	444	375	0.25	0.10
C₆m-Bg-r2	50.3	79.9	71.1	0.21	0.0363	0.5	1.3	452	333	0.45	0.31
C₈m-Bg	52.6	80.3	66.0	0.26	0.0065	3.3	2.0	173	123	0.12	0.07
C₂m-C	49.0	79.4	72.9	0.23	0.0012	0.3	1.9	842	514	0.81	0.59
C₄m-C	47.9	76.9	72.1	0.23	0.0024	0.5	1.5	747	559	0.51	0.27
C₆m-C	44.9	75.0	74.3	0.20	0.0011	0.5	2.5	611	451	0.51	0.32
C₈m-C	42.6	70.9	67.6	0.15	0.0152	3.6	7.6	266	149	0.28	0.21
(Bn)m-Bg	66.5	110.3	70.0	0.19	0.0082	4.7	2.9	294	118	0.49	0.44
(Bn)m-Bg-S	66.1	105.2	70.7	0.22	0.0071	2.5	0.3	433	241	0.68	0.35
(Bn)b-Bg	72.0	121.6	72.0	0.17	0.0045	3.3	3.4	6	4	n/a	n/a
(Bn)b-Bg-S	66.1	107.6	72.8	0.24	0.0006	1.5	0.4	14	6	0.02	0.02
(Bn)₂-Bg	127.6	256.2	71.5	0.06	0.0295	10.8	9.0	7	1	0.02	0.02
(Bn)₂-Bg-S	114.4	208.1	78.1	0.07	0.0179	3.3	2.4	25	4	0.07	0.07
HTC-Bg	39.1	60.3	70.4	0.26	0.0019	0.0	0.0	24	7	0.00	0.09
Na-Bg	46.2	63.2	56.1	0.43	0.0032	6.1	3.9	168	123	0.05	0.12
K-Bg	42.9	63.9	66.7	0.38	0.0003	1.3	0.7	733	697	0.29	0.04
P350-Bg	22.9	34.3	68.4	0.17	0.0037	n/a	n/a	16	15 (315)^h	0.01 (0.12)^h	0.00
P550-Bg	17.5	31.0	80.9	0.08	0.0041	n/a	n/a	384	384 (470)^h	0.16 (0.18)^h	0.00
P750-Bg	16.7	30.3	82.8	0.09	0.0018	n/a	n/a	392	389 (588)^h	0.17 (0.22)^h	0.01

^{a} Y_{mc} for corrected mass yield. ^{b} Y_c for carbon yield. ^{c} Weight percentages obtained from elemental analyses. ^{d} Molar ratios obtained from elemental analyses. ^{e} SEM-EDX analyses. ^{f} Determined from nitrogen sorption isotherms at 77 K using the t-plot method. ^{g} Determined from the amount of nitrogen adsorbed at a relative pressure of 0.99. ^{h} Equivalent micropore surface area and micropore volume determined from carbon dioxide sorption isotherms at 273 K using the Dubinin–Astakhov equation.

above 280 °C.[37] The yield of recovered ILs after ITC was about 96 wt% both for **C₂m-Bg** and **C₆m-Bg**, which is in good agreement with the ones determined in a previous study for the ITC of cocoa bean shells in [Bmim]FeCl₄ at 240 °C for 20 h (*ca.* 95 wt%).[30] The IL loss was mainly due to the tetrachloroferrate anion, with residual iron and chlorine in the ionochars ranging from 4 to 7 wt% (Table 1). To assess their reusability, two ILs of the [C$_x$mim]FeCl₄ series, *i.e.*, [C₂mim]FeCl₄ and [C₆mim]FeCl₄, were recycled twice, yielding **C$_x$m-Bg-r1** and **C$_x$m-Bg-r2**. After each ITC cycle, the yield of recovered IL was maintained between 92 and 98 wt%. Moreover, both the mass and carbon yields reached for **C$_x$m-Bg-r1** and **C$_x$m-Bg-r2** remained relatively high, above 48 and 75 wt% respectively (Table 1). Despite a 5 to 10% decrease in the micropore contribution after each cycle, the textural properties obtained for **C$_x$m-Bg-r1** and **C$_x$m-Bg-r2** are really close to the ones obtained for the ionochars after the first ITC cycle (Table 1 and Fig. S4†). However, one may notice a 25 to 50% increase in pore volume (*ca.* 0.2 cm³ g⁻¹) from **C$_x$m-Bg-r1** to **C$_x$m-Bg-r2**. We believe that these features are due to iron loss with each ITC cycle, which might change the nature of the chloroferrate anions. In this respect, we are currently conducting a study to better understand the role of the anion speciation in the ITC of sugarcane bagasse in imidazolium chloroferrate ILs.

Moreover, pyrolysis and, to a lesser extent, HTC gave lower carbonization yields as compared with ITC (Table 1). This behavior is particularly relevant for the pyrochar prepared at 350 °C, namely **P350-Bg**, which displays an elemental composition similar to the analogous hydro- and ionochars (*i.e.*, with a carbon content of 68.4 wt% and O/C molar ratio of 0.17; Table 1). The mass and carbon yields reached to prepare **P350-Bg** are half as efficient as the ones reached by ITC. This feature confirms the atom-economical character of ITC compared to more conventional carbonization approaches. At this stage, it is important to note that the relevance of the ITC approach depends closely on the selected IL. In a previous study Wang *et al.*[31] performed the ITC of sugarcane bagasse in 1-(3-cyanopropyl)-3-methylimidazolium chloride, [BCNmim]Cl, at 200 °C for 24 hours. The authors obtained a ionochar with significantly lower BET-equivalent specific surface area (35 m² g⁻¹), pore volume (0.15 cm³ g⁻¹) and mass yield (37 wt%) as compared with the ones reported herein. Besides, [BCNmim]Cl is unstable and could not be reused due to partial degradation, which resulted in nitrogen-doping of the ionochar with a nitrogen content of 6.6 wt%. This feature further emphasizes the applicative interest of short-chain imidazolium tetrachloroferrate ILs for the ITC of lignocellulosic biomass and agrowastes.

Besides textural properties and carbonization yields, significant differences were observed in terms of molecular structures between pyrochars, hydrochar and ionochars. The FTIR spectrum of **HTC-Bg** shows a clear dissimilitude compared to the ones of the four ionochars of the **C$_x$m-Bg** series (Fig. 3b). Three new bands were observed for **HTC-Bg**. The two sharp bands centered at 1504 and 1110 cm⁻¹ correspond to the aromatic $\nu_{C=C}$ stretching vibrations of lignin and the ν_{C-O-C} stretching vibrations of ether groups of holocellulose (*i.e.*, the
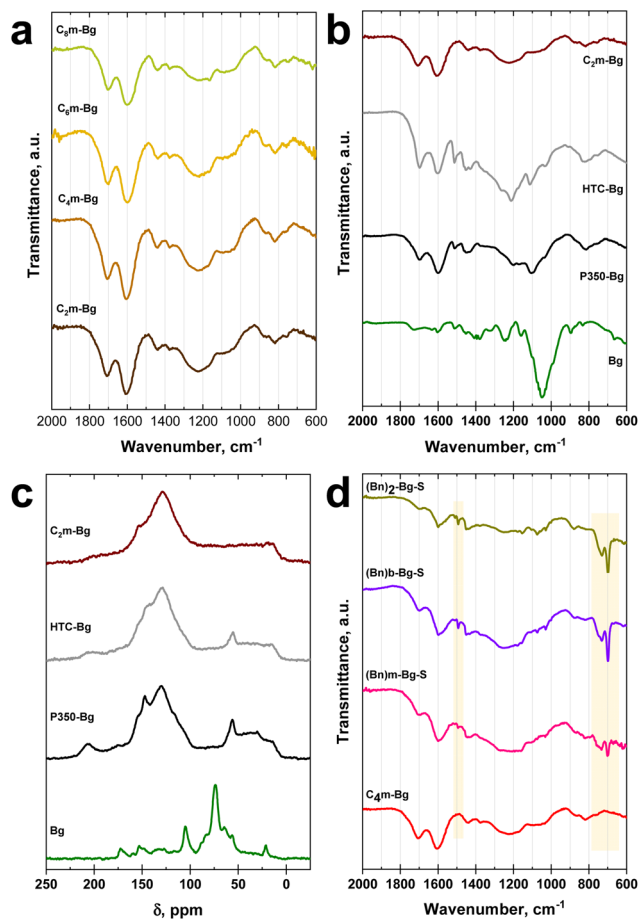
Fig. 3 FTIR spectra of (a) the four ionochars of the **C$_x$m-Bg** series; (b) **C$_2$m-Bg**, **HTC-Bg**, **P350-Bg** and raw sugarcane bagasse, **Bg**. (c) ^{13}C CP-MAS solid-state NMR spectra of **C$_2$m-Bg**, **HTC-Bg**, **P350-Bg** and raw sugarcane bagasse, **Bg**. (d) FTIR spectra of **(Bn)m-Bg-S**, **(Bn)b-Bg-S**, **(Bn)$_2$-Bg-S** (after soxhlet extraction) and **C$_4$m-Bg**.

carbohydrate fraction of sugarcane bagasse), respectively. The weak shoulder centered at 1040 cm^{-1} can correspond to the in plane deformation of the C–H bonds (δ_{CH}) in the aromatic rings of lignin. Moreover, the bands centered at 1440 cm^{-1} and between 1220 and 1280 cm^{-1} are more intense than for the four ionochars of the **C$_x$m-Bg** series. These features confirm that, whatever the alkyl chain length, ITC in 1-alkyl-3-methylimidazolium tetrachloroferrate ILs favors the deconstruction/carbonization of lignin. Interestingly, the FTIR spectrum of **P350-Bg** (Fig. 3b), which is the pyrochar with the elemental composition that is the closest to the analogous hydro- and ionochars, is very similar to the one obtained for **HTC-Bg**. This feature was also confirmed by Raman spectroscopy (Fig. S5†) and ^{13}C solid-state NMR (Fig. 3c). The ^{13}C solid-state NMR spectrum of raw sugarcane bagasse (**Bg**) displays the signature of lignocellulose with the characteristic peaks of cellulose centered at 65 (C6), 72–75 (C2, C3, C5), 84–89 (C4) and 105 ppm (C6) and hemicellulose centered at 20–25 and 70–75 ppm. After carbonization, the characteristic peaks of holocellulose disappeared. Two major domains can

be clearly identified: the aliphatic region between 0 and 65 ppm and the aromatic region centered at 129 ppm. The ^{13}C solid-state NMR spectra of **HTC-Bg** and **P350-Bg** show clear differences compared to the ones of the four ionochars of the **C$_x$m-Bg** series: two peaks centered at 55–56 ppm and 147–148 ppm can be observed. As reported by Baccile *et al.*,[40] the peak centered at 55–56 ppm can be attributed to residual methoxy groups of lignin, while the peak centered at 147–148 ppm can be attributed to aromatic carbons in *ipso* position to methoxy groups of lignin. Note that the shoulder centered at 151 ppm can be attributed to the presence of polyfuranic aromatic structures coming from the thermochemical degradation of cellulose. We also performed Raman spectroscopy to provide additional information on the molecular structure of the materials. The Raman spectra of the four ionochars of the **C$_x$m-Bg** series are similar to that of **P350-Bg** (Fig. S5a†) and are typical of amorphous carbonaceous structures with a significant fraction of sp^3-hybridized carbon atoms. Interestingly, the Raman spectrum of **HTC-Bg** shows stronger fluorescence with a significant deviation of the baseline (Fig. S5b†). This behavior may be attributed to the highest presence of auxochromes in the polyfuranic aromatic structures of **HTC-Bg**, due to a lower carbonization rate compared to the ionochars and **P350-Bg**. To conclude on this part, FTIR, ^{13}C solid-state NMR and Raman spectroscopy confirm the beneficial character of ITC for the efficient degradation of lignin and carbonization of lignocellulose. This feature is probably due to the catalytic role of the tetrachloroferrate anions as shown in recent studies.[20,30]

To confirm the effect of the alkyl chain length in 1-alkyl-3-methylimidazolium tetrachloroferrate ILs on textural properties, a similar study was carried out with commercial cellulose, which is the main constituent of bagasse. Comparable trends were observed (Fig. S6 and Table S4†). The SSA$_{BET}$ and the pore volume gradually increase from 266 m^2 g^{-1} and 0.28 cm^3 g^{-1} for **C$_8$m-C** to 842 m^2 g^{-1} and 0.81 cm^3 g^{-1} for **C$_2$m-C**. In the same way as for bagasse, no significant variation was observed for both mass (between 42.6 and 49.0 wt%) and carbon yields (between 70.9 and 79.4 wt%) (Fig. S6d and Table S5†). These features strongly suggest that the structure of the imidazolium cation plays a major role in the way (ligno) cellulose and IL interact and assemble during ITC. In the literature, the role of the cation in the dissolution of cellulose in IL was first neglected.[24,41,42] The major driving force for cellulose dissolution can be attributed to the formation of hydrogen bonds between the anion of the IL and the hydroxyl groups of cellulose. Although still open to debate, the interactions between cellulose and the imidazolium cation are assumed to involve van der Waals forces rather than hydrogen-bonding.[43–46] Chu *et al.*[47] showed that the protons of the imidazolium cations strongly interact with side-chain and linker oxygen atoms of cellulose. Zhang *et al.* showed that the presence of long alkyl chains in [C$_x$mim]Cl has a negative impact on the dissolution of cellulose, mainly due to steric hindrance.[23] The longer the alkyl chain length, the fewer the anions surrounding the cellulose and the weaker the inter-

molecular interactions between the anion and the cellulose. As the length of the alkyl chain increases, the ability of $[C_x\text{mim}]$ Cl to dissolve cellulose becomes weaker[23] and aggregates will tend to form in the medium for $x > 8$.[48,49] Besides, as the length of the alkyl chain in $[C_x\text{mim}]\text{FeCl}_4$ increases, both the fluidity and the Walden product of the IL decrease, due to pronounced van der Waals attraction between the alkyl chains.[37] One may assume that the cation undoubtedly has a role in (ligno)cellulose dissolution.[17,44,50,51] In our work, the results observed with the $[C_x\text{mim}]\text{FeCl}_4$ (with $x = 2, 4, 6,$ or 8) series for the ITC of both cellulose and bagasse seem to follow the same trend as the $[C_x\text{mim}]$Cl series for the dissolution of cellulose. Thus, the fact that $[C_2\text{mim}]\text{FeCl}_4$ leads to ionochars with the highest SSA_{BET} and pore volumes might be due to stronger interactions between (ligno)cellulose and IL.

To further support the role of the cation, ITC of bagasse was also carried out in imidazolium tetrachloroferrate ILs carrying one or two benzyl groups (Fig. 1a), *i.e.*, $[(\text{Bn})\text{mim}]\text{FeCl}_4$, $[(\text{Bn})\text{bim}]\text{FeCl}_4$ and $[(\text{Bn})_2\text{im}]\text{FeCl}_4$. The as-obtained ionochars were named **(Bn)m-Bg**, **(Bn)b-Bg** and **(Bn)₂-Bg**, respectively. These ILs are rather unstable during ITC, especially $[(\text{Bn})_2\text{im}]$ FeCl_4, as the benzyl side groups are subject to Hofmann eliminations. This feature has been evidenced by elemental analyses, FTIR and EDX performed on ionochars (Fig. 3d and Table S6†) and GC-MS and FTIR carried out on recovered ILs after ITC (Fig. S7 and S8†). In particular, the FTIR spectra of the three ionochars obtained after Soxhlet extraction, samples named **(Bn)m-Bg-S**, **(Bn)b-Bg-S** and **(Bn)₂-Bg-S**, display two intense bands between 690 and 730 cm^{-1}, which are characteristic of the deformation of =C–H bonds ($\delta_{=C-H}$), together with a weaker band centered at 1500 cm^{-1}, characteristic of the stretching vibration of C=C bonds ($\nu_{C=C}$). Thus, the presence of residual benzyl (Fig. 3d and Fig. S7†) and imidazole (Table S6 and Fig. S7†) moieties in these ionochars was clearly evidenced, even after Soxhlet extraction. Moreover, GC-MS of $[(\text{Bn})_2\text{im}]\text{FeCl}_4$ recovered after ionothermal carbonization of bagasse at 240 °C for 20 h revealed the presence of 1-benzylimidazole (Fig. S7†). Our previous statement, positioning ITC as a potentially sustainable approach in terms of environmental factor and atom economy, is therefore directly dependent on the IL used and cannot be generalized to 1-benzylimidazolium-based ILs.

Besides chemical instability considerations, we showed that the structure of the 1-benzylimidazolium-based cation has a direct impact on the textural properties of the ionochar. In the same way as for the **C$_x$m-Bg** series, the cation with the shorter alkyl chain length leads to the ionochar ((**Bn)m-Bg**) with the highest SSA_{BET} (433 m^2 g^{-1}) and pore volume (0.68 cm^3 g^{-1}; Fig. S9 and Table S7†). Note that, due to partial degradation of these three ILs during ITC, both mass and carbon yields are significantly overestimated, in particular for **(Bn)₂-Bg** and **(Bn)₂-Bg-S** (above 100%). The grafting of benzyl groups onto ionochars cannot be excluded. Thus, we decided not to discuss the mass and carbon yields obtained for the three corresponding ionochars (Table S6†).

To provide better insight into the role of the cationic structure, ITC in imidazolium tetrachloroferrate ILs was also compared with ITC in tetrachloroferrate salts bearing cheap and abundant alkali metals, *i.e.*, NaFeCl_4 and KFeCl_4. The as-obtained ionochars were named **Na-Bg** and **K-Bg**. On the one hand, **Na-Bg** displays a type I/II isotherm similar to the ones obtained for the **C$_x$m-Bg** series (Fig. S10a†). Both SSA_{BET} (168 m^2 g^{-1}) and pore volume (0.17 cm^3 g^{-1}) are close to the ones obtained for **C$_8$m-Bg** (Table 1, Fig. S10b, c and Table S8†). On the other hand, **K-Bg** displays a type I(a) isotherm typical of microporous materials with narrow micropores (Fig. S10a†), yielding a high SSA_{BET} of 733 m^2 g^{-1} and a pore volume of 0.33 cm^3 g^{-1} (Table 1 and Table S8†). An increase in the cation size from Na to K leads to a significant increase in microporosity. However, the contribution of the external pore volume is limited as compared with the **C$_x$m-Bg** series (Fig. 2c). The mass (42.9 wt% for **K-Bg**; 46.2 wt% for **Na-Bg**) and carbon yields (63.9 wt% for **K-Bg**; 63.2 wt% for **Na-Bg**) for these two ionochars are slightly higher than those of **HTC-Bg** (39.1 wt% and 60.3 wt% respectively) (Table 1, Fig. S10d and Table S9†). They are, however, significantly lower than those obtained by ITC in the $[C_x\text{mim}]\text{FeCl}_4$ series, confirming the benefit of cation engineering of the IL for ITC of (ligno)cellulose.

So far, we demonstrated that the nature and the constitution of the cation can be favorable to design advanced porous ionochars in terms of textural properties (high SSA_{BET} and pore volumes) and atom-economy (high mass and carbon yields). Interestingly, we also showed a fine control in terms of morphological properties (Fig. 3a and b). Firstly, significant differences were observed in the **C$_x$m-Bg** series. The two ionochars prepared in ILs with short alkyl chain lengths, *i.e.*, **C$_2$m-Bg** and **C$_4$m-Bg**, are made of aggregates of small nanoparticles. SEM and TEM images reveal interparticle void spaces forming an interconnected pore network made of large mesopores and narrow macropores. This feature is in good agreement with the data extracted from the nitrogen sorption analyses (Fig. 2 and Table 1). As discussed earlier, the strong intermolecular interactions between ILs bearing short alkyl chains and lignocellulose favor lignin depolymerization, most probably through the cleavage of the γ-O ester and β-O-4 ether bonds.[52–54] Then, cellulose is readily accessible for further dissolution, deconstruction and homogeneous solvothermal carbonization, yielding highly porous ionochars made of small nanoparticles. When increasing the alkyl chain length, very different morphologies were obtained (Fig. 4c and d). Thus, for **C$_6$m-Bg** and **C$_8$m-Bg**, bundles of large amorphous nanotubes with an external diameter of *ca.* 100 to 300 nm are observed. Note that the inner diameter of the tubes was clearly identified by TEM, confirming the hollow nature of the particles (Fig. 3c₂–d₂). Unlike bagasse, no tubular nanostructures were observed with cellulose (Fig. S11†). In the light of the previous discussion regarding lignocellulose dissolution in ILs, one may assume that the laborious dissolution/deconstruction of lignin in $[C_6\text{mim}]\text{FeCl}_4$ and $[C_8\text{mim}]\text{FeCl}_4$ offers a limited lignocellulose–solvent interface preventing complete depolymerisation. As a direct consequence, it is likely that the carbonization occurred in a heterogeneous solid–liquid biphasic
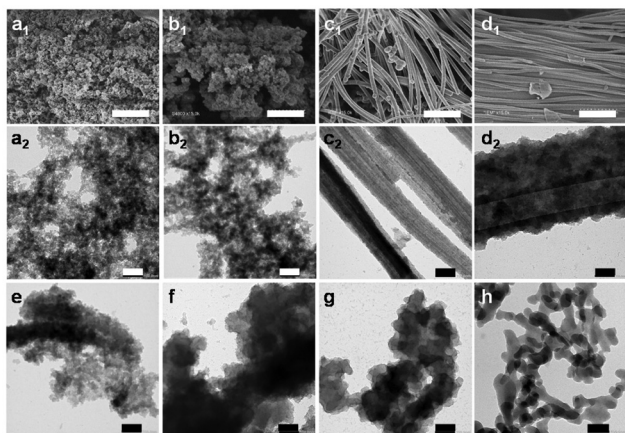
Fig. 4 Micrographs obtained by scanning (a_1-d_1; scale bar 2 µm) and transmission (a_2-d_2; scale bare 100 nm) electron microscopy of (a) C_4m-Bg, (b) C_4m-Bg, (c) C_6m-Bg and (d) C_8m-Bg. Micrographs obtained by transmission electron microscopy of (e) **(Bn)m-Bg**, (f) **(Bn)b-Bg**, (g) **(Bn)$_2$-Bg** and (h) **HTC-Bg**. Scale bar: 100 nm.

medium through intramolecular reactions, thus preserving the fibrous structure of fibrils in lignocellulose and yielding a carbonaceous replica made of bundles of large nanotubes.

In view of the results obtained with cellulose, it is unlikely that such tubular structures result from a self-assembly of the IL itself. Surprisingly, no tubular nanostructures were observed in **C$_6$m-Bg-r1** and **C$_6$m-Bg-r2**. As mentioned previously, we believe that these features are due to iron loss with each ITC cycle, which might change the nature of the chloroferrate anions in the IL and its intermolecular interactions with lignocellulose. Interestingly, TEM performed on **(Bn)m-Bg**, **(Bn)b-Bg** and **(Bn)$_2$-Bg** did not show any tubular structures despite substantial steric hindrance on the cation, and the anticipation of a limited ability to dissolve lignocellulose. Instead, stacked nanoplatelets were observed, particularly for the two ionochars obtained in the bulkiest cations, *i.e.*, **(Bn)b-Bg** and **(Bn)$_2$-Bg** (Fig. 4e–g). One may assume that the presence of benzyl group (s) onto the cation promotes π–π type interactions with lignin and with the subsequent ionochars, which might favor the formation of two-dimensional stacked nanoplatelets. Despite the limited stability of the (Bn)-containing ILs, the textural and morphological properties of the resulting ionochars give interesting insights into their specific interactions with bagasse during ITC. We are currently studying other polyphenolic biomolecules and natural extracts to further support this hypothesis. Note that the micrographs of **HTC-Bg** reveal the aggregation of nonporous large nanoparticles of *ca.* 100 nm in diameter (Fig. 4h). No exotic morphologies, neither nanotubes nor nanoplatelets, were observed.

Due to advantageous textural and morphological properties, the ionochars reported herein can find applications in various fields, including catalysis, wastewater treatment,[55] energy storage[29] and environmental remediation.[31] In our previous study, ITC and as-obtained ionochars demonstrated beneficial inputs for gas sorption, especially for post combustion carbon

dioxide (CO_2) capture.[31] Herein, we confirm that the four ionochars of the **C$_x$m-Bg** series outperform the analogous hydro- and pyrochars, *i.e.*, **HTC-Bg** and **P350-Bg** (Fig. 5a). Interestingly, we show that cation engineering can significantly improve the CO_2 uptake, *i.e.*, the quantity of CO_2 adsorbed per gram of ionochar (Fig. 5a). At 273 K and 100 kPa, the CO_2 uptake increases from 1.6 mmol of CO_2 per gram for **C$_8$m-Bg** to 2.2 mmol of CO_2 per gram for **C$_2$m-Bg** (which corresponds to a 37% increase). Similar features were observed at 298 and 323 K (Fig. S12†). Interestingly, we show that cation engineering may also offer the possibility to control the specific affinity of the ionochar for CO_2 adsorption; in other words, its ability not only to capture, but also to retain CO_2. Thus, the isosteric heat of adsorption of each ionochar was calculated for the **C$_x$m-Bg** series applying the Clausius–Clapeyron equation to CO_2 adsorption isotherms obtained at three different temperatures (Fig. S13†). It appears that the isosteric heat of adsorption increases by *ca.* 10% (*ca.* 3 kJ mol^{-1}) from **C$_2$m-Bg** to **C$_6$m-Bg** (Fig. 5b). While **C$_2$m-Bg** has the higher CO_2 uptake, it dis-
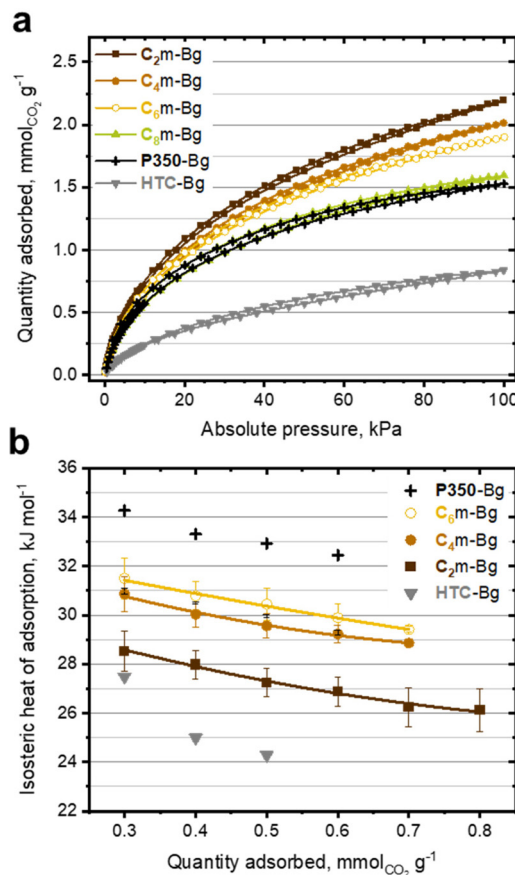
Fig. 5 (a) Carbon dioxide sorption isotherms at 273 K of **C$_2$m-Bg**, **C$_4$m-Bg**, **C$_6$m-Bg**, **C$_8$m-Bg**, **P350-Bg** and **HTC-Bg**. (b) Isosteric heat of adsorption of CO_2 for **HTC-Bg**, **C$_2$m-Bg**, **C$_4$m-Bg**, **C$_6$m-Bg** and **P350-Bg**. The isosteric heat of adsorption was calculated by applying the Clausius–Clapeyron equation to CO_2 adsorption isotherms obtained at three different temperatures (273, 298 and 323 K). Note that the isosteric heats of adsorption are given as absolute values. The corresponding isosteric enthalpies of adsorption are negative.

plays the lower affinity for CO_2; thus, lower energy would be required to fully desorb CO_2. Moreover, the isosteric heats of adsorption calculated for the ionochars of the **C$_x$m-Bg** series are intermediate between the analogous hydro- and pyrochars (Fig. 5b), supporting significant differences in terms of micropore size distribution and surface chemistry. These features confirm the high versatility and singularity of the ITC process, especially through cation engineering, to design advanced carbonaceous materials with unusual properties.

4. Conclusions

In summary, we demonstrate the possibility to control both textural and morphological properties of ionochars through cation engineering. We prepared a series of imidazolium tetrachloroferrate ILs bearing modular side groups, *e.g.*, alkyl chains with different lengths and/or benzyl groups. We applied ITC to a lignocellulosic agrowaste (*i.e.*, sugarcane bagasse) and commercial cellulose. We showed the reusability of two different 1-alkyl-3-methylimidazolium tetrachloroferrate ILs over three ITC cycles. When decreasing the alkyl chain length from octyl to ethyl in 1-alkyl-3-methylimidazolium tetrachloroferrate ILs, both BET-equivalent specific surface area (SSA_{BET}) and total pore volume gradually increased up to 800 m^2 g^{-1} and 0.8 cm^3 g^{-1}, respectively. When increasing the alkyl chain length, lower SSA_{BET} and total pore volume were obtained, but singular tubular nanostructures with an external diameter of *ca.* 100 to 300 nm were observed. Besides, the formation of two-dimensional stacked nanoplatelets was observed for the ionochars prepared in imidazolium tetrachloroferrate ILs carrying one or two benzyl groups. While still open to discussion, the cation undoubtedly has a role in (ligno)cellulose dissolution, deconstruction and ionothermal carbonization. Finally, we show that cation engineering also offers the possibility to control both the CO_2 uptake and retention of ionochars. Due to advantageous and adjustable properties offered by cation engineering, we expect that our study will open new opportunities for the ITC of (ligno) cellulose. We are currently studying potential applications in various fields, including catalysis, wastewater treatment and energy storage.

Author contributions

S. A.: Investigation, writing – original draft. M. E.-S., S. K. and P. H.: Validation, writing – review & editing. N. B. and A. M.: Conceptualization, funding acquisition, supervision, validation, writing – review & editing.

Conflicts of interest

There are no conflicts to declare.

Acknowledgements

References

1 X.-F. Tan, Y.-G. Liu, Y.-L. Gu, Y. Xu, G.-M. Zeng, X.-J. Hu, S.-B. Liu, X. Wang, S.-M. Liu and J. Li, *Bioresour. Technol.*, 2016, **212**, 318–333.

2 D. A. Iryani, S. Kumagai, M. Nonaka, K. Sasaki and T. Hirajima, *Waste Biomass Valorization*, 2017, **8**, 1941–1951.

3 S. Katyal, K. Thambimuthu and M. Valix, *Renewable Eng.*, 2003, **28**, 713–725.

4 A. K. Varma and P. Mondal, *Ind. Crops Prod.*, 2017, **95**, 704–717.

5 Y. Guo, C. Tan, J. Sun, W. Li, J. Zhang and C. Zhao, *Chem. Eng. J.*, 2020, **381**, 122736.

6 S. A. Nicolae, H. Au, P. Modugno, H. Luo, A. E. Szego, M. Qiao, L. Li, W. Yin, H. J. Heeres and N. Berge, *Green Chem.*, 2020, **22**, 4747–4800.

7 G. Ischia and L. Fiori, *Waste Biomass Valorization*, 2021, **12**, 2797–2824.

8 M.-M. Titirici and M. Antonietti, *Chem. Soc. Rev.*, 2010, **39**, 103–116.

9 M. Sevilla, A. B. Fuertes and R. Mokaya, *Energy Environ. Sci.*, 2011, **4**, 1400–1410.

10 T. P. Fellinger, R. J. White, M. M. Titirici and M. Antonietti, *Adv. Funct. Mater.*, 2012, **22**, 3254–3260.

11 M. Volpe, A. Messineo, M. Mäkelä, M. R. Barr, R. Volpe, C. Corrado and L. Fiori, *Fuel Process. Technol.*, 2020, **206**, 106456.

12 P. Zhang, Y. Gong, H. Li, Z. Chen and Y. Wang, *Nat. Commun.*, 2013, **4**, 1–11.

13 Z. G. Lei, B. H. Chen, Y. M. Koo and D. R. MacFarlane, *Chem. Rev.*, 2017, **117**, 6633–6635.

14 H. Wang, G. Gurau and R. D. Rogers, *Chem. Soc. Rev.*, 2012, **41**, 1519–1537.

15 C. Chiappe and D. Pieraccini, *J. Phys. Org. Chem.*, 2005, **18**, 275–297.

16 S. Aldroubi, N. Brun, I. B. Malham and A. Mehdi, *Nanoscale*, 2021, **13**, 2750–2779.

17 R. P. Swatloski, S. K. Spear, J. D. Holbrey and R. D. Rogers, *J. Am. Chem. Soc.*, 2002, **124**, 4974–4975.

18 A. Salama and P. Hesemann, *ACS Sustainable Chem. Eng.*, 2020, **8**, 17893–17907.

19 Y. Zhou, X. Zhang, D. Yin, J. Zhang, Q. Mi, H. Lu, D. Liang and J. Zhang, *Green Chem.*, 2022, **24**, 3824–3833.

20 Z. Li, Z. Cai, Q. Zeng, T. Zhang, L. J. France, C. Song, Y. Zhang, H. He, L. Jiang and J. Long, *Green Chem.*, 2018, **20**, 3743–3752.

21 M. J. Mehta, A. Kulshrestha, S. Sharma and A. Kumar, *Green Chem.*, 2021, **23**, 1240–1247.

22 F. Ferrari, G. Nogueira, T. Franco, M. Dias, C. Cavaliero, G. J. Witkamp, L. Van Der Wielen and M. B. S. Forte, *Green Chem.*, 2021, **23**, 9126–9139.

23 Y. Zhao, X. Liu, J. Wang and S. Zhang, *ChemPhysChem*, 2012, **13**, 3126–3133.

24 R. C. Remsing, R. P. Swatloski, R. D. Rogers and G. Moyna, *Chem. Commun.*, 2006, 1271–1273.

25 Z.-L. Xie, R. J. White, J. Weber, A. Taubert and M. M. Titirici, *J. Mater. Chem.*, 2011, **21**, 7434–7442.

26 X.-X. Lin, B. Tan, L. Peng, Z.-F. Wu and Z.-L. Xie, *J. Mater. Chem. A*, 2016, **4**, 4497–4505.

27 J. S. Lee, R. T. Mayes, H. Luo and S. Dai, *Carbon*, 2010, **48**, 3364–3368.

28 M. Baccour, N. Louvain, J. G. Alauzun, L. Stievano, P. H. Mutin, B. Boury, L. Monconduit and N. Brun, *J. Power Sources*, 2020, **474**, 228575.

29 Y. Liu, B. Huang, X. Lin and Z. Xie, *J. Mater. Chem. A*, 2017, **5**, 13009–13018.

30 L. Cibien, M. Parot, P. N. Fotsing, P. Gaveau, E. D. Woumfo, J. Vieillard, A. Napoli and N. Brun, *Green Chem.*, 2020, **22**, 5423–5436.

31 P. Zhang, Y. Gong, Z. Wei, J. Wang, Z. Zhang, H. Li, S. Dai and Y. Wang, *ACS Appl. Mater. Interfaces*, 2014, **6**, 12515–12522.

32 S. Hayashi, S. Saha and H.-O. Hamaguchi, *IEEE Trans. Magn.*, 2005, **42**, 12–14.

33 J.-Y. Kim, J.-T. Kim, E.-A. Song, Y.-K. Min and H.-O. Hamaguchi, *Macromolecules*, 2008, **41**, 2886–2889.

34 S. Hayashi and H.-O. Hamaguchi, *Chem. Lett.*, 2004, **33**, 1590–1591.

35 D. Yin, C. Li, L. Tao, N. Yu, S. Hu and D. Yin, *J. Mol. Catal. A: Chem.*, 2006, **245**, 260–265.

36 K. Bica and P. Gaertner, *Org. Lett.*, 2006, **8**, 733–735.

37 Y. Yoshida and G. Saito, *J. Mater. Chem.*, 2006, **16**, 1254–1262.

38 W. E. Dunn, Jr., *United States of America Pat*, US3729543A, 1973.

39 T. Bäcker, O. Breunig, M. Valldor, K. Merz, V. Vasylyeva and A.-V. Mudring, *Cryst. Growth Des.*, 2011, **11**, 2564–2571.

40 C. Falco, N. Baccile and M.-M. Titirici, *Green Chem.*, 2011, **13**, 3273–3281.

41 R. C. Remsing, G. Hernandez, R. P. Swatloski, W. W. Massefski, R. D. Rogers and G. Moyna, *J. Phys. Chem. B*, 2008, **112**, 11071–11078.

42 J. S. Moulthrop, R. P. Swatloski, G. Moyna and R. D. Rogers, *Chem. Commun.*, 2005, 1557–1559.

43 J. Zhang, H. Zhang, J. Wu, J. Zhang, J. He and J. Xiang, *Phys. Chem. Chem. Phys.*, 2010, **12**, 1941–1947.

44 T. Youngs, C. Hardacre and J. Holbrey, *J. Phys. Chem. B*, 2007, **111**, 13765–13774.

45 M. J. Earle, J. M. Esperança, M. A. Gilea, J. N. Canongia Lopes, L. P. Rebelo, J. W. Magee, K. R. Seddon and J. A. Widegren, *Nature*, 2006, **439**, 831–834.

46 R. C. Remsing, I. D. Petrik, Z. Liu and G. Moyna, *Phys. Chem. Chem. Phys.*, 2010, **12**, 14827–14828.

47 H. M. Cho, A. S. Gross and J.-W. Chu, *J. Am. Chem. Soc.*, 2011, **133**, 14033–14041.

48 J. Wang, H. Wang, S. Zhang, H. Zhang and Y. Zhao, *J. Phys. Chem. B*, 2007, **111**, 6181–6188.

49 M. Blesic, M. H. Marques, N. V. Plechkova, K. R. Seddon, L. P. N. Rebelo and A. Lopes, *Green Chem.*, 2007, **9**, 481–490.

50 Y. Fukaya, K. Hayashi, M. Wada and H. Ohno, *Green Chem.*, 2008, **10**, 44–46.

51 A. Xu, J. Wang and H. Wang, *Green Chem.*, 2010, **12**, 268–275.

52 T. Y. Kim, H. W. Lee, M. Stoller, D. R. Dreyer, C. W. Bielawski, R. S. Ruoff and K. S. Suh, *ACS Nano*, 2011, **5**, 436–442.

53 T. Zhang, Y. Zhang, Y. Wang, F. Huo, Z. Li, Q. Zeng, H. He and X. Li, *Front. Chem.*, 2019, 446.

54 F. S. Chakar and A. J. Ragauskas, *Ind. Crops Prod.*, 2004, **20**, 131–141.

55 Z.-L. Xie, X. Huang, M.-M. Titirici and A. Taubert, *RSC Adv.*, 2014, **4**, 37423–37430.